Structural and optoelectronic behavior of the copper-doped Cs$_2$AgInCl$_6$ double perovskite: A density functional theory investigation

Isaac Busayo Ogunniranye [1,*], Tersoo Atsue [1,2] and Oluwole Emmanuel Oyewande [1,†]

[1]*Theoretical Physics Unit, Department of Physics, Faculty of Science, University of Ibadan, Ibadan, Nigeria*
[2]*Department of Physics, Faculty of Physical Science, Federal University Dutsin-Ma, Katsina, Nigeria*

Recently, direct band gap double perovskites have become more popular among the photovoltaic research community owing to their potential to address issues of lead toxicity and structural instability inherent in lead halide (simple) perovskites. In this study, an In-Ag-based direct band gap double perovskite, Cs$_2$AgInCl$_6$ (CAIC), is treated with transition metal doping to improve the optoelectronic properties of the material. Investigations of the structural and optoelectronic properties of Cu-doped CAIC, Cs$_2$Ag$_{(1-x)}$Cu$_x$InCl$_6$, are done using *ab initio* calculations with density functional theory and virtual crystal approximation. Our calculations show that with increasing Cu content, the optimized lattice parameter and direct band gap of Cs$_2$Ag$_{(1-x)}$Cu$_x$InCl$_6$ decrease following linear and quadratic functions, respectively, while the bulk modulus increases following a quartic polynomial function. The photoabsorption coefficient, optical conductivity, and other optical parameters of interest are also computed, and the obtained spectra indicate enhanced optical properties at higher Cu contents. Based on our results, transition metal (Cu) doping is a viable means of treating double perovskites, by tuning their optoelectronic properties to be suitable for an extensive range of photovoltaics, solar cells, and optoelectronics.

I. INTRODUCTION

Perovskite-based solar cells (PSCs) have recently been promoted as a renewable technology option for conventional solar cell technology capable of tackling global energy demands and climate change challenges owing to their economic and environmental viability [1]. Their emergence as one of the most promising emerging technologies has aroused the interest of the photovoltaic community, owing to their increasing power conversion efficiency from 3.8% in 2009 [2] to 25.2% [3], materials availability, low production cost, and ease of the fabrication process [4–10].

One of the core elements governing PSC performance is perovskite materials, typically CH$_3$NH$_3$PbI$_3$ or MAPbI (methyl ammonium lead triiodide), serving both as light harvesters and charge carrier mediators [2,5,11]. Over the years, numerous studies have shown MAPbI to possess appealing qualities needed for photovoltaic and optoelectronic applications, such as a suitable band gap ($\sim$1.5 eV), good photoconductivity, considerable lifetime diffusion length ($>$100 μm), high optical absorption coefficient, great bipolar transporting capability, defect tolerance ability, and low carrier effective masses with high mobility [12–25]. Despite having these exceptional properties, MAPbI still faces some fundamental issues, such as structural instability, toxicity associated with lead, photocurrent hysteresis, and scalability [26–31], which have hampered their large-scale commercialization as viable PSCs.

Several attempts have been made to address the most fundamental issues of instability and toxicity inherent in halide perovskites, such as multication substitution, hydrophobic moiety incorporation (e.g., hydrophobic polymers), surface passivation of a perovskite absorber, carbon encapsulation, a low-dimensionality scheme or treatment, and lead replacement with nontoxic elements [26,32–38]. Reports have shown that (i) substituting Pb with nontoxic group IVA elements (Sn, Ge) results in chemical instability and poor device performance owing to oxidation to their 4+ states [39–42] and (ii) substituting it with isovalent elements (Bi, Sb) leads to reduced device efficiency [43]. This has thus created the need to develop novel classes of materials that are capable of tackling the instability and toxicity issues while still retaining the appealing properties of the Pb-based halide perovskites (LHPs).

As of late, double perovskites (DPs) are beginning to gain popularity in the photovoltaic community owing to their ability to tackle issues of Pb toxicity and structural instability [44,45]. A DP is represented by the general $A_2M'M''X_6$ stoichiometry, where A denotes a large cation like Cs or Rb, M' and M'' represent monovalent and trivalent cations, respectively ($M' = $ Ag$^+$, Cu$^+$, Na$^+$; $M'' = $ In^{3+}, Bi^{3+}), and X indicates a halide ($X = $ Cl$^-$, I$^-$, Br$^-$) [44,45]. The material properties of cation-ordered and vacancy-ordered DPs have been investigated experimentally and theoretically to determine their suitability for photovoltaic and optoelectronic applications. Research findings have shown that most DPs exhibit considerable thermal and mechanical stability compared to Pb-based halide perovskites but possess a large band gap with an indirect nature, which has limited their usage in solar cell applications [44,46–49].

*Corresponding author: ib.ogunniranye@ui.edu.ng
†Corresponding author: oe.oyewande@ui.edu.ng

Given this, attention is now drawn to direct band gap DPs. Direct band gap DPs are at the forefront following the pioneering work by Volonakis and coworkers in 2017 in which the $Cs_2AgInCl_6$ (CAIC) DP was proposed, synthesized, and identified as a potential, environmentally benign replacement for Pb-based halide perovskites for photovoltaic and other optoelectronic applications [50]. CAIC is a direct band gap DP with high thermal and mechanical stability, which crystallizes in the fcc structure with space group $Fm\bar{3}m$ and has an experimental lattice parameter of 10.469–10.481 Å and band gap of 2.5–3.3 eV [50–52]. These have made CAIC of huge research interest and a potential alternative for LHPs. However, pure bulk CAIC crystal or powder is characterized by a low photoluminescence quantum yield (PLQY) and photoabsorption coefficient compared to CAIC nanocrystals (NCs), and these are a result of parity-induced forbidden transition [51,53–55]. In the quest to tune and optimize the optoelectronic properties of DPs, experimental findings have identified doping engineering as a viable way to achieve this and thus having the potential of enabling their widespread usability beyond photovoltaic applications [56,57]. Very recently, reports showed the synthesis of a doped CAIC NC, treated with transition (Mn) and posttransition (Bi) metals, exhibiting high PLQYs, enhanced photoabsorption, and other related optical properties when compared with pure CAIC in either powder or NC form [53,58–60].

Numerical simulation has widespread application for a variety of problems [61–63]. In particular, Monte Carlo simulation and mathematical modeling have been widely applied in the quest for more cost-effective fabrication of devices [64–74], whereas properties of new materials have been studied with quantum-mechanical calculations using density functional theory for decades [38,45,75]. However, theoretical studies based on density functional theory (DFT) on M-cation doping in double perovskites are scarce. In a recent study, Jiao and associates used a DFT scheme to investigate material properties of the metal-alloying DP $Cs_2AgM_xBr_6$ (M_x = Sb, In, Bi), where indirect to direct band gap transition was observed [76]. Transition metal (TM) doping can lead to the enhancement of material properties, especially their optoelectronic properties. Since Cu and Ag are both TMs and isovalent cations, the former is used as the dopant for this study. Previous studies have shown Cu doping to be effective in enhancing the photoluminescence and thermoelectric properties of materials [77,78].

Based on the scope of our literature search, Cu doping in CAIC has yet to be explored both theoretically and experimentally. Consequently, this paper seeks to investigate the effect of Cu doping on the structural and optoelectronic properties of CAIC ($Cs_2Ag_{(1-x)}Cu_xInCl_6$) using the virtual crystal approximation (VCA) approach within the framework of DFT. VCA is a first-principles technique in modeling disordered solid solutions via pseudopotential averaging and is effective in treating disordered systems [79–81]. This work focuses on only the bulk optoelectronic properties of perovskite materials.

The remainder of this paper is organized in the following order. In Sec. II, the computational methods employed for the calculations are described. Section III is devoted to the presentation and discussion of our results. Finally, a brief summary of the work is given.

II. COMPUTATIONAL METHODS

In this work, the *ab initio* calculations for CAIC and $Cs_2Ag_{(1-x)}Cu_xInCl_6$ (CAIC:Cu) solid solutions are performed using the pseudopotential plane-wave technique based on DFT as implemented in the QUANTUM ESPRESSO (QE) software package [82,83]. Within the framework of DFT, the structural and optoelectronic properties with the electronic exchange-correlation (XC) potential are calculated using the Perdew-Burke-Ernzerhof (PBE) functional [84] based on the generalized gradient approximation (GGA). To circumvent PBE band gap underestimation arising from self-interaction error, the hybrid PBE0 functional [85] is employed to treat the electronic exchange-correlation potential for the calculations of band structures.

For the electron-ion interaction, the optimized normconserving Vanderbilt (ONCV) pseudopotentials [86] are used for all calculations and construction of the virtual atoms ($Ag_{(1-x)}$-Cu_x). The VCA method [79,80] is used to generate the pseudopotentials of the virtual atoms ($Ag_{(1-x)}$-Cu_x), where the mixing ratio x is varied from 0 to 1 in steps of 0.1. The plane-wave energy cutoff of 100 Ry and Monkhorst-Pack special [87] k points of $8 \times 8 \times 8$ are used for optimization calculations and the calculations of the electronic band structure and optical properties, while denser k points of $12 \times 12 \times 12$ are used for density of states (DOS) calculations. While the convergence threshold for the self-consistent-field iteration is set at 10^{-10} eV, the Broyden-Fletcher-Goldfarb-Shanno minimization method [88] is employed for the geometry optimization of the perovskites. All atomic positions are relaxed until the Helmann-Feynman forces on each atom become less than 20 meV/Å.

To examine the optical properties of the perovskites, density functional perturbation theory (DFPT) [89–91] as implemented in QE is used to determine the complex frequency-dependent dielectric functions $\varepsilon(\omega)$:

$$\varepsilon(\omega) = \varepsilon_1(\omega) + i\varepsilon_2(\omega). \tag{1}$$

From Eq. (1), ω denotes the photon frequency, and $\varepsilon_1(\omega)$ and $\varepsilon_2(\omega)$ are the real and imaginary parts of the dielectric function $\varepsilon(\omega)$, respectively. The dielectric functions are computed using the GGA-PBE approximation. To determine the light-harvesting capability of the perovskites, the absorption coefficient $\alpha(\omega)$ is calculated using

$$\alpha(\omega) = \frac{\sqrt{2}\omega}{c}\sqrt{[\mathbf{K} - \varepsilon_1(\omega)]}, \tag{2}$$

where

$$\mathbf{K} = \sqrt{\varepsilon_1^2(\omega) + \varepsilon_2^2(\omega)}.$$

Other optical parameters of interest are optical conductivity, the refractive index, the extinction coefficient, and the energy-loss function. The optical conductivity $\sigma(\omega)$ and

TABLE I. Perovskite formability factors for $Cs_2AgInCl_6$ and CAIC:Cu solid solutions. Here x is the mixing ratio in steps of 0.1 ($0 < x < 1$).

Material	μ	t	τ
CAIC ($x = 0$)	0.54	0.94	−4.79
$Cs_2(Cu_xAg_{1-x})InCl_6$	0.44–0.53	0.94–1.00	−2.74 to −2.48
CCIC ($x = 1$)	0.43	1.01	−2.73

refractive index $n(\omega)$ of the materials are computed, respectively, using the relations

$$\sigma(\omega) = \frac{\omega \varepsilon_2}{4\pi}, \tag{3}$$

$$n(\omega) = \frac{1}{\sqrt{2}} \sqrt{[\mathbf{K} + \varepsilon_1(\omega)]}. \tag{4}$$

In terms of the complex dielectric function in Eq. (1), the extinction coefficient $k(\omega)$ and the energy-loss function $L(\omega)$ are determined, respectively, using

$$k(\omega) = \frac{1}{\sqrt{2}} \sqrt{[\mathbf{K} - \varepsilon_1(\omega)]}, \tag{5}$$

$$L(\omega) = \frac{\varepsilon_2(\omega)}{\mathbf{K}^2}. \tag{6}$$

III. RESULTS AND DISCUSSION

A. Formability evaluation

A typical double-perovskite structure is defined by the general $A_2M'M''X_6$ stoichiometry. In this work, the metal cation in the crystallographic A site is taken to be Cs, the transition metal cation $M' = $ Ag, Cu, $Ag_{(1-x)}Cu_x$, and the posttransition metal cation $M'' = $ In, while the halide $X = $ Cl. To assert the crystallographic stability of the CAIC:Cu solid solutions' structure, the perovskite formability parameters are computed using

$$\mu = \frac{(r_{M'} + r_{M''})}{2r_X}, \tag{7}$$

$$t = \frac{(r_A + r_X)}{\sqrt{2}\left[\frac{(r_{M'} + r_{M''})}{2} + r_X\right]}, \tag{8}$$

$$\tau = \frac{2r_X}{(r_{M'} + r_{M''})} - n_A\left(n_A - \frac{2r_A/(r_{M'} + r_{M''})}{\ln[2r_A/(r_{M'} + r_{M''})]}\right), \tag{9}$$

where μ, t, and τ are octahedral, Goldschmidt's tolerance, and new tolerance factors, respectively. r_A, $r_{M'}$, $r_{M''}$, and r_X denote the Shannon radii [92] for the corresponding ions, and n_A is the oxidation number of A. For stable perovskite structures, the ideal ranges for μ, t, and τ are $0.44 \leqslant \mu \leqslant 0.9$, $0.81 \leqslant t \leqslant 1.11$, and $\tau < 4.18$, respectively [45,93–95]. As presented in Table I, the results predict that CAIC and the Cu-doped $Cs_2AgInCl_6$ solid solutions can form stable three-dimensional perovskite structures, except for the pure Cu-based compound $Cs_2CuInCl_6$ (CCIC) with an octahedral factor (0.43) slightly less than the lower limit of μ. These formability factors are not sufficient enough to assert the material's feasibility and stability.

Recent studies have shown CAIC is thermodynamically stable, while its Cu counterpart (CCIC) is unstable [50,96].
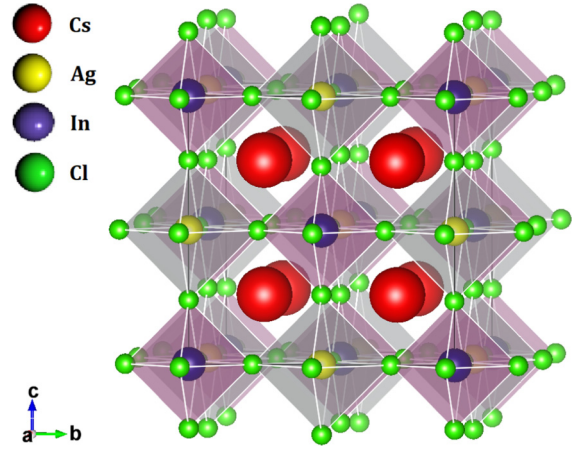

FIG. 1. Polyhedral view of the $Cs_2AgInCl_6$ double perovskite (space group $Fm\bar{3}m$).

This intrinsic instability in the Cu(I)-based double perovskite was attributed to the high energy level associated with the $3d$ state of Cu [96]. Despite this, the pure Cu-based compound is examined for the purpose of comparing its properties with those of CAIC and CAIC:Cu solid solutions. The thermodynamic stability of the Ag-Cu solid solutions with respect to the formation of domains of the pristine CAIC and the pure Cu-based compound CCIC is discussed in the next section.

B. Structural properties

The host perovskite, CAIC, crystallizes in the fcc phase with a space group of $Fm\bar{3}m$, and its crystalline structure is illustrated in Fig. 1. The polyhedral view of CAIC was generated using VESTA [97]. Within the framework of DFT, the lattice parameter a and bulk modulus B_0 of the host perovskite are calculated by fitting the total energy–unit cell volume (E-V) data into the Birch-Murnaghan equation of state [98]. Following Han *et al.*, who reported that the van der Waals (vdW) functional is actually preferred for accurate description of the lattice parameter of inorganic halide double perovskites [99], we used the vdW functional to calculate the lattice parameter and found that for the double-perovskite CAIC, which is the focus of this work, the result (10.5 Å) obtained is on the same order of magnitude as that obtained with the PBE functional (10.6 Å) when compared with experimental values (10.5 Å [50,51]). Hence, we use the PBE functional for all calculations.

GGA-PBE slightly overestimates the lattice parameter for the host perovskite. However, the computed optimized lattice parameter for the host perovskite is comparable with experimental values [50,51]. The above procedure is repeated for $Cs_2Ag_{(1-x)}Cu_xInCl_6$ while varying the Cu content x from 0 to 1 in steps of 0.1. To ascertain the reliability of the VCA method, the lattice parameter and electronic band gap of $Cs_2(Cu_{0.5}Ag_{0.5})InCl_6$ are computed using a $2 \times 2 \times 2$ supercell. From Table II, the results show an appreciable level of agreement. However, a comparison of the lattice parameter computed within the VCA and the supercell approach suggests slight deviations from linearity.

TABLE II. Lattice parameter a and electronic band gap E_g of the $Cs_2(Cu_{0.5}Ag_{0.5})InCl_6$ solid solution calculated within different alloying approaches: virtual crystal approximation and supercell (SC).

Method	This work	
	VCA	SC
a(Å)	10.55	10.59
E_g (eV)	0.44	0.34

Figure 2(a) shows the optimized lattice parameters and bulk moduli of CAIC:Cu solid solutions. To illustrate the compositional dependence of the computed lattice parameters, we interpolate the computed lattice parameter to a linear function of Cu content x, which gives the relation $a(x) = 10.6297 - 0.1659x$. This relation follows Vegard's law—a consequence of the alloying scheme. From Fig. 2(a), the lattice parameter a decreases with increasing Cu content x, an indication that the addition of Cu dopant will cause the crystal lattice of the pristine CAIC to shrink. This may be attributed to the large difference in ionic radii between Cu (0.77 Å) and Ag (1.15 Å). Conversely, the bulk modulus B_0 of Cu-doped CAIC tends to
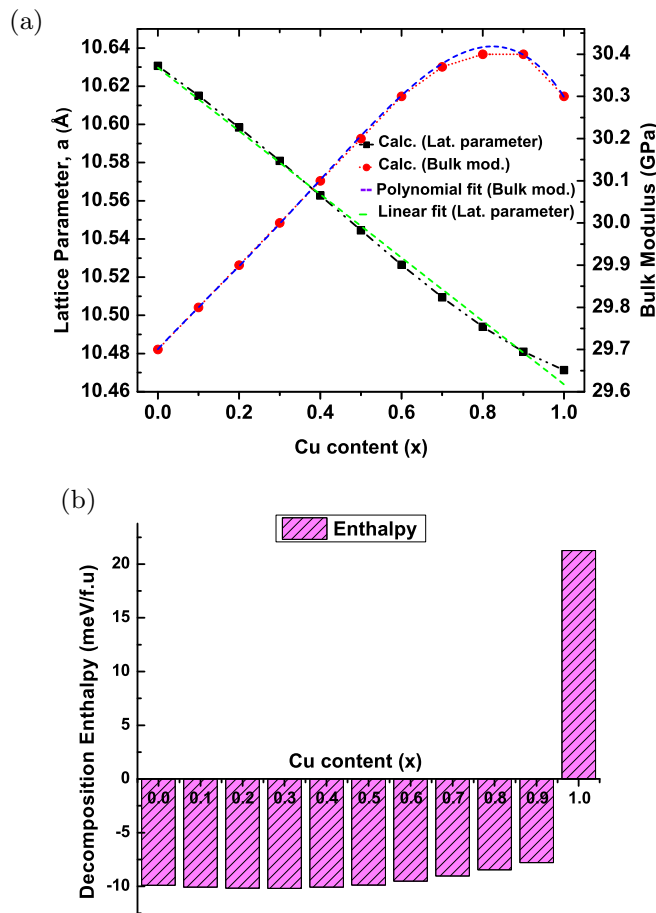

(a)

(b)

FIG. 2. (a) Calculated lattice parameters and bulk moduli as a function of Cu content x in CAIC:Cu solid solutions. Linear and polynomial fittings are presented. (b) Decomposition enthalpies ΔH for CAIC and the CAIC:Cu solid solutions.

increase following the quartic polynomial function $B_0(x) = 29.7007 + 1.0272x - 0.5070x^2 + 1.8260x^3 - 1.7483x^4$.

C. Material stability

Beyond the crystallographic formability evaluation, the materials' stability is imperative for their design, fabrication, and commercialization. To assess the intrinsic stability of the alloyed configuration of CAIC using the PBE XC functional, we compute the decomposition enthalpy ΔH from the total energies with respect to a possible decomposition pathway: $2Cs_2AgInCl_6 \rightleftharpoons Cs_3In_2Cl_9 + CsCl + 2AgCl$. The decomposition enthalpies ΔH for the double perovskites are computed as the total energy difference between the perovskite and its compositions, given by

$$\Delta H = 2E_T[\text{CAIC:Cu}] - E_T[Cs_3In_2Cl_9]$$
$$- E_T[CsCl] - 2E_T[Ag_{(1-x)}Cu_xCl] \quad (10)$$

where E_T denotes the DFT total energy of the corresponding compounds. For the decomposition enthalpy calculations, well-relaxed systems are employed. The assumed crystal structures for $Cs_3In_2Cl_9$, CsCl, and AgCl are trigonal (R-$3c$), cubic ($Fm\bar{3}m$), and cubic ($Fm\bar{3}m$), respectively. As depicted in Fig. 2(b), the computed decomposition enthalpies are negative for CAIC and CAIC:Cu solid solutions and positive for CCIC. The results suggest CAIC and CAIC:Cu solid solutions are thermodynamically stable. Conversely, the positive enthalpy value for CCIC suggests it is thermodynamically unstable. This is consistent with previous reports on CCIC [50,96].

D. Electronic properties

In this section, DFT based on the *ab initio* calculations is used to examined the electronic structures of CAIC and CAIC:Cu solid solutions. From DFT calculations, GGA-PBE is first employed as the XC functional for the band structure calculations. The calculated band gap of CAIC (1.00 eV) is observed to be about 70% underestimated compared with the experimental values (3.3 eV [50], 3.23 eV [51]). Negative band gap values are obtained for CAIC:Cu at $x = 0.8, 0.9$ and CCIC ($x = 1$) with GGA-PBE. To circumvent this underestimation and improve the accuracy of the band gap, the hybrid PBE0 is used as the XC functional, and a band gap value of 3.27 eV is obtained, which is in agreement with the experimental value of Volonakis *et al.* [50].

To assess the spin-orbit coupling (SOC) effect in CAIC, we compute PBE and PBE0 band structures with or without the SOC contribution and obtain band gap values of 1.01 and 3.29 eV, respectively. The difference between the calculated band gaps with and without SOC using PBE and PBE0 functionals is ~0.01 and ~0.02, respectively. Table III shows the comparative results of the calculated band gap with other experimental and theoretical results. Comparing these values to those obtained with PBE and hybrid PBE0 shows that the inclusion of SOC has an insignificant effect on the electronic properties of CAIC and may be ignored. This is in agreement with previous reports [50,101]. Hence, for further calculations, the SOC effect is ignored.

TABLE III. Calculated electronic band gap E_g of the CAIC and CCIC double perovskites using different exchange-correlation functionals (with or without the inclusion of SOC) compared with other experimental and theoretical results.

		This work				Previous work	Expt.
	Material	PBE	PBE+SOC	PBE0	PBE0+SOC		
E_g (eV)	CAIC ($x=0$)	1.00	1.01	3.27	3.29	2.9–3.3 [50], 3.33 [51]	3.3 [50], 3.23 [51]
	CCIC ($x=1$)	−0.03		2.39		1.05[a] to 1.73[b] [100]	

[a]Heyd-Scuseria-Ernzerhof (HSE06) + SOC.
[b]PBE0 + SOC.

The nature of the band gap, as well as the positions of the valence band minimum (VBM) and the conduction band maximum (CBM), can be revealed via the electronic band structure. Figure 3(a) shows the electronic band structure of CAIC (host perovskite) along some selected high-symmetry points, which reflect that CAIC is a direct band gap DP with

(a)

(b)

FIG. 3. (a) Calculated PBE0 electronic band structure and total and partial densities of states of the host perovskite, Cs$_2$AgInCl$_6$. (b) Total and partial DOSs for CAIC:Cu solid solutions.

both CBM and VBM located at the Γ point in the Brillouin zone. To ascertain the atomic orbital contributions towards the electronic states at the CBM and VBM, the total and partial DOSs are calculated. Figure 3(a) shows the PBE0 total and partial densities of states for CAIC where VBM is set at zero. From Fig. 3(a), the Ag $4d$ and Cl $3p$ states dominate the valence bands, while the In $5s$ states exclusively dominate the conduction bands.

Given the above, it is worth noting that the hybrid PBE0 functional can give the most reliable band gap value for double perovskites (see Table III). With this assertion, the hybrid PBE0 functional is then used to calculate the electronic band structure of CAIC:Cu solid solutions. Figure 4 shows the variation tendency in the band gap as the Cu content x increases. By interpolating the band gaps to a polynomial function, the band gaps are observed to decrease quadratically with a function of $E(x) = 3.3277 - 0.8757x - 0.2868x^2$, with increasing Cu content x. Based on Vegard's law, this function can be reduced to

$$E_g(x) = E_g(0) + [E_g(1) - E_g(0) - b]x + bx^2, \quad (11)$$

where $E_g(0)$ and $E_g(1)$ denote the band gap of CAIC ($x = 0$) and CCIC ($x = 1$), respectively, while b represents the band gap bowing parameter. From our results, $E_g(0) = 3.3277$ eV, $E_g(1) = 2.1652$ eV, and $b = -0.2868$ eV. The band gap
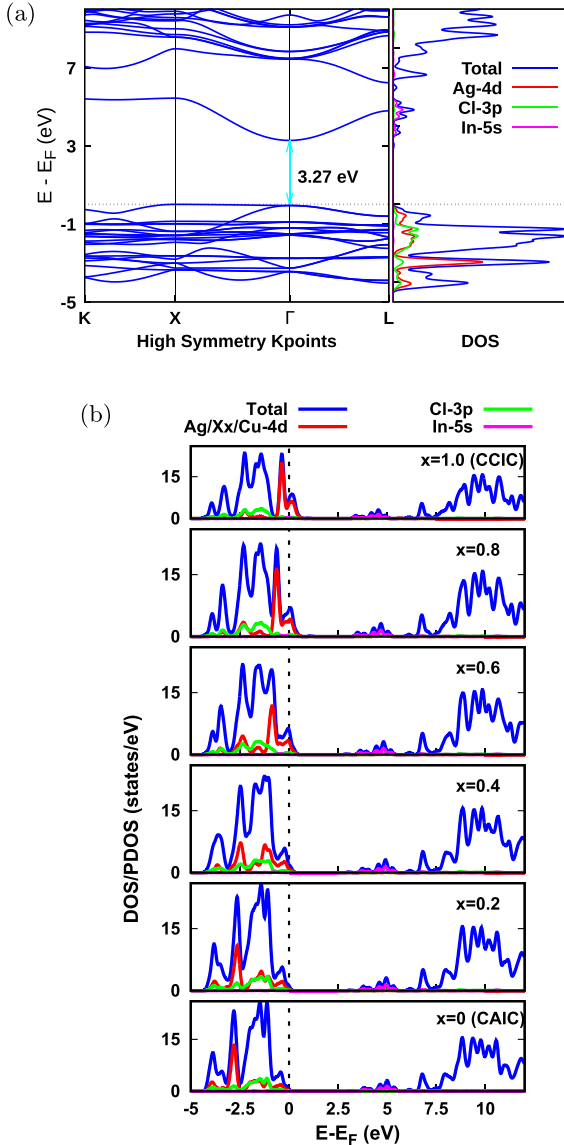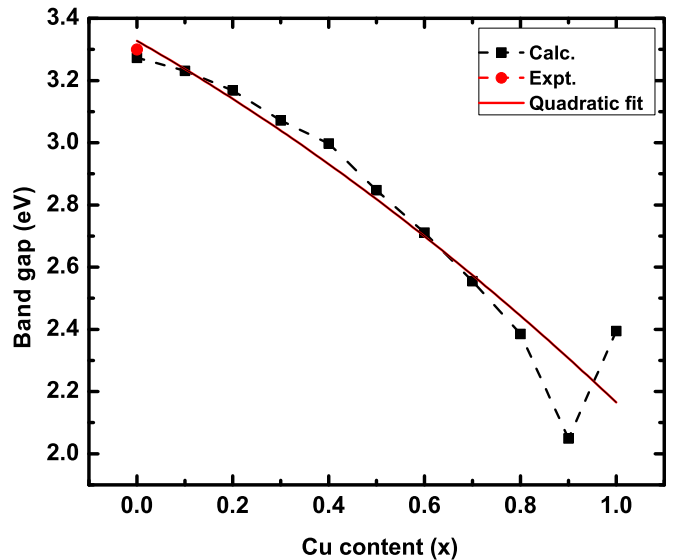

FIG. 4. Electronic band gaps of CAIC:Cu solid solutions as a quadratic function of Cu content x. The experimental band gap value of CAIC is presented.

bowing parameter b indicates the nonlinearity of the band gap to the composition, as well as the degree of fluctuation in the crystal field.

These results suggest enhancement of the light-absorbing capability of the materials owing to the reduction in the band gap with increasing Cu content. The band gap decrement can be attributed to the average energy of the Cu d states, as illustrated in Fig. 3(b). Comparing the band gap of the 50:50 supercell and the VCA value (see Table II) suggests an appreciable level of miscibility between CAIC and CCIC and small compositional disorder.

Meng and coworkers, in a recent DFT study, attributed the wide optical band gap of $Cs_2AgInCl_6$ to parity-forbidden transitions, which can be traced to the DP centrosymmetry and the unoccupied In $5s$ orbitals in the lowest conduction band [55]. With the analysis of the band symmetry and parity, the addition of Cu does not change the number of parity-forbidden transitions and the band gap nature of Cu-doped CAIC, an indication that Cu dopant does not influence the symmetry of the band edges of Cu-doped CAIC.

E. Optical properties

In this section, the optical properties of the materials are calculated using the ONCV pseudopotentials [86] and the complex frequency-dependent dielectric functions $\varepsilon(\omega)$ as given in Eq. (1). At the single-particle level, the complex frequency-dependent dielectric functions are computed within the random phase approximation using the GGA-PBE approximation. The exciton binding energy is small in silicon, and excitonic effects may be negligible in that case and not for this perovskite host. Excitonic effects may be required to correctly compute matrix elements and capture prominent features in the linear absorption spectrum. It is quite difficult to obtain excitons with time-independent DFT as most standard XC functionals lack the long-range property [102]. In a more elaborate consideration of such effects one may use YAMBO codes [103], which are now available, and experimental approaches based on excited-state spectroscopies such as ultrafast spectroscopy and two-step excitation techniques, among others. However, phonon-based transitions and excitonic effects are not the focus of this study. To quantify the effects of Cu doping on the optical properties, the photoabsorption coefficients, optical conductivity, and other optical properties of interest are calculated and presented.

These quantities can be understood, in general, in a vein similar to statistical physics principles of response functions. There a specific response of a system measured as a change in some characteristic quantity of the system (a so-called generalized force) relative to some known stimulus (generalized displacement) is used to determine the nature and suitability of the system in relation to desired applications.

One of the key parameters that determine the power conversion efficiency of PSCs and other related optoelectronic devices is the photoabsorption coefficient [Fig. 5(a)]. The photoabsorption coefficient gives one good insight into the light-harvesting capability of a material. It can be estimated using Eq. (2) with the real and imaginary parts of the complex frequency-dependent dielectric functions. Note that the material's optical band gaps are underestimated at the PBE
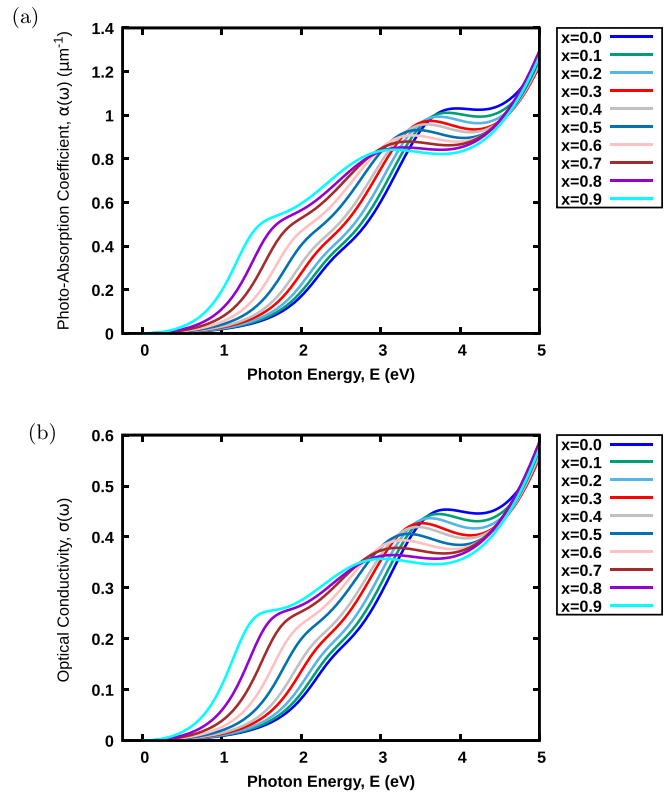

FIG. 5. (a) Calculated photoabsorption coefficients and (b) optical conductivity for Cu-doped CAIC double perovskites at the PBE level.

level. Figure 5(a) shows the variation of the photoabsorption coefficients for CAIC and CAIC:Cu solid solutions as a function of photon energy. The absorption onset for $Cs_2AgInCl_6$ quite agrees with the fundamental band gap extracted from the PBE band structure. Within the visible range (1.5–3.1 eV), the photoabsorption coefficients steadily increase with energy. In comparison with CAIC, increased photoabsorption coefficients are notably observed across the whole visible range with increasing Cu content x. However, the results for CCIC are not plotted because PBE predicts this material is metallic.
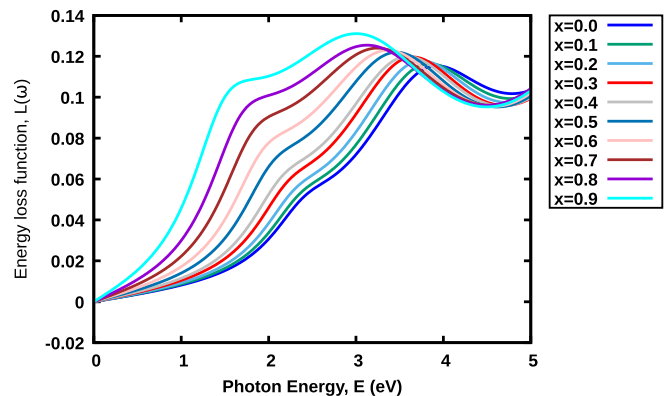

FIG. 6. Calculated energy-loss function $L(\omega)$ for CAIC:Cu solid solutions.
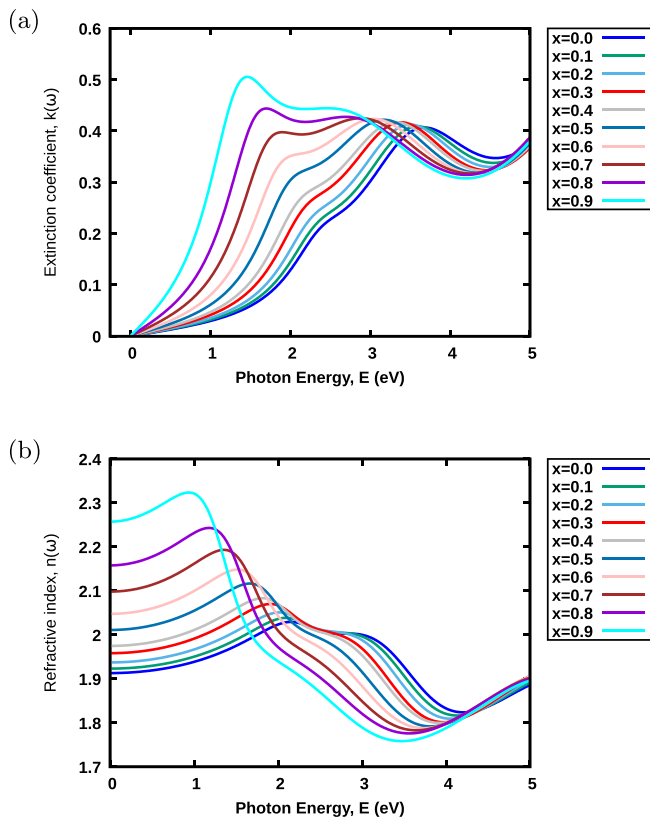
(a)

(b)

FIG. 7. Variation in the calculated (a) extinction coefficient $k(\omega)$ and (b) refractive index $n(\omega)$ as a function of energy for CAIC:Cu solid solutions.

Furthermore, the optical conductivity [Fig. 5(b)], a measure of susceptibility to light, of the material is also examined. The variation tendency of the calculated optical conductivity of the materials is presented in Fig. 5(b). A trend similar to the variation of absorption coefficients is observed. Another important optical parameter is the energy-loss function (Fig. 6), which is used to describe the energy loss due to fast-moving electrons in the material. From the calculated spectra in Fig. 6, the electron energy-loss increases with the Cu content, and characteristic peaks are observed between 2.8 and 3.4 eV for the materials.

Also, the extinction coefficient [Fig. 7(a)] and refractive index [Fig. 7(b)] are important optical parameters used to predict materials' suitability for device applications beyond photovoltaic. The former determines the amount of absorption loss, while the latter describes the phase velocity when electromagnetic waves propagate through the materials. Figures 7(a) and 7(b) show the variation of the calculated

extinction coefficient and refractive index as a function of energy. Within the visible range, the calculated extinction coefficients increase with increasing concentration of Cu content in CAIC. In comparison, CAIC:Cu at $x = 0.9$ shows a peak value of ~ 0.5 between 1.3 and 1.6 eV. Similarly, the static refractive index of the materials increases with the Cu content, while CAIC:Cu at $x = 0.9$ displays a peak value of ~ 2.32 between 0.8 and 1.0 eV. The findings of this study have shown Cu, a transition metal, to be an efficient dopant in treating a double perovskite, as it enhances the material optoelectronic properties.

It is hoped that the present work will invite experimental synthesis and study and that such study would be promising enough to motivate more accurate calculations that would include excitonic effects and use the elaborate methodology for handling them.

IV. CONCLUSION

In this work, the effect of Cu doping on the structural and optoelectronic properties of CAIC was studied using first-principles DFT calculations and the VCA approach. The *ab initio* VCA method was used to model the solid solutions. The PBE0 functional was used for the band structure calculations after assessing the exchange-correlation functional of GGA-PBE. With increasing Cu content, the crystal lattice shrinks following a linear function, $a(x) = 10.6297 - 0.1659x$; the bulk modulus increases with the quartic polynomial function $B_0(x) = 29.7007 + 1.0272x - 0.5070x^2 + 1.8260x^3 - 1.7483x^4$, while the band gap decreases quadratically with a function of $E(x) = 3.3277 - 0.8757x - 0.2868x^2$. The photoabsorption coefficient, optical conductivity, and other optical parameters of interest were calculated using the DFPT method. The spectra obtained show enhancement in the optical properties of the materials with higher Cu contents. The variation tendencies, as a result of Cu doping, in the structural and optoelectronic properties of the materials under study have shown Cu is an efficient dopant in treating double perovskites. This work presents $Cs_2Ag_{(1-x)}Cu_xInCl_6$ (CAIC:Cu) solid solutions as potential candidates for photovoltaics and optoelectronics.

[1] T. Ibn-Mohammed, S. C. Koh, I. M. Reaney, A. Acquaye, G. Schileo, K. B. Mustapha, and R. Greenough, Renewable Sustainable Energy Rev. **80**, 1321 (2017).

[2] A. Kojima, K. Teshima, Y. Shirai, and T. Miyasaka, J. Am. Chem. Soc. **131**, 6050 (2009).

[3] National Renewable Energy Laboratory (NREL), Best Research-Cell Efficiency Chart (2020), https://www.nrel.gov/pv/cell-efficiency.html.

[4] H. J. Snaith, J. Phys. Chem. Lett. **4**, 3623 (2013).

[5] M. Liu, M. B. Johnston, and H. J. Snaith, Nature (London) **501**, 395 (2013).

[6] J. Burschka, N. Pellet, S.-J. Moon, R. Humphry-Baker, P. Gao, M. K. Nazeeruddin, and M. Grätzel, Nature (London) **499**, 316 (2013).

[7] N.-G. Park, J. Phys. Chem. Lett. **4**, 2423 (2013).

[8] F. Di Giacomo, S. Razza, F. Matteocci, A. D'Epifanio, S. Licoccia, T. M. Brown, and A. Di Carlo, J. Power Sources **251**, 152 (2014).

[9] S. Casaluci, L. Cinà, A. Pockett, P. S. Kubiak, R. G. Niemann, A. Reale, A. Di Carlo, and P. Cameron, J. Power Sources **297**, 504 (2015).

[10] J. Liu, J. Lin, Q. Xue, Q. Ye, X. He, L. Ouyang, D. Zhuang, C. Liao, H.-L. Yip, J. Mei, and W.-M. Lau, J. Power Sources **301**, 242 (2016).

[11] A. M. Ganose, C. N. Savory, and D. O. Scanlon, Chem. Commun. **53**, 20 (2017).

[12] H.-H. Fang, R. Raissa, M. Abdu-Aguye, S. Adjokatse, G. R. Blake, J. Even, and M. A. Loi, Adv. Funct. Mater. **25**, 2378 (2015).

[13] T. Baikie, Y. Fang, J. M. Kadro, M. Schreyer, F. Wei, S. G. Mhaisalkar, M. Graetzel, and T. J. White, J. Mater. Chem. A **1**, 5628 (2013).

[14] S. D. Stranks, G. E. Eperon, G. Grancini, C. Menelaou, M. J. P. Alcocer, T. Leijtens, L. M. Herz, A. Petrozza, and H. J. Snaith, Science **342**, 341 (2013).

[15] T. Hakamata, K. Shimamura, F. Shimojo, R. K. Kalia, A. Nakano, and P. Vashishta, Sci. Rep. **6**, 19599 (2016).

[16] J. Even, L. Pedesseau, J.-M. Jancu, and C. Katan, J. Phys. Chem. Lett. **4**, 2999 (2013).

[17] S. D. Stranks and H. J. Snaith, Nat. Nanotechnol. **10**, 391 (2015).

[18] R. Watanabe and H. Noji, Nat. Commun. **5**, 3486 (2014).

[19] T. C. Sum and N. Mathews, Energy Environ. Sci. **7**, 2518 (2014).

[20] E. Edri, S. Kirmayer, S. Mukhopadhyay, K. Gartsman, G. Hodes, and D. Cahen, Nat. Commun. **5**, 3461 (2014).

[21] A. Walsh, D. O. Scanlon, S. Chen, X. G. Gong, and S.-H. Wei, Angew. Chem., Int. Ed. **54**, 1791 (2015).

[22] Y. Shao, Z. Xiao, C. Bi, Y. Yuan, and J. Huang, Nat. Commun. **5**, 5784 (2014).

[23] J. M. Frost, K. T. Butler, F. Brivio, C. H. Hendon, M. van Schilfgaarde, and A. Walsh, Nano Lett. **14**, 2584 (2014).

[24] R. Lindblad, D. Bi, B.-w. Park, J. Oscarsson, M. Gorgoi, H. Siegbahn, M. Odelius, E. M. J. Johansson, and H. Rensmo, J. Phys. Chem. Lett. **5**, 648 (2014).

[25] Q. Lin, A. Armin, R. C. R. Nagiri, P. L. Burn, and P. Meredith, Nat. Photonics **9**, 106 (2015).

[26] M. Shahbazi and H. Wang, Sol. Energy **123**, 74 (2016).

[27] Z. Li, T. R. Klein, D. H. Kim, M. Yang, J. J. Berry, M. F. A. M. van Hest, and K. Zhu, Nat. Rev. Mater. **3**, 18017 (2018).

[28] J. S. Manser, M. I. Saidaminov, J. A. Christians, O. M. Bakr, and P. V. Kamat, Acc. Chem. Res. **49**, 330 (2016).

[29] P. Zhang, J. Yang, and S.-H. Wei, J. Mater. Chem. A **6**, 1809 (2018).

[30] S. Chatterjee and A. J. Pal, J. Mater. Chem. A **6**, 3793 (2018).

[31] G. Niu, X. Guo, and L. Wang, J. Mater. Chem. A **3**, 8970 (2015).

[32] C. Wu, H. Li, Y. Yan, B. Chi, K. M. Felice, R. B. Moore, B. A. Magill, R. R. H. H. Mudiyanselage, G. A. Khodaparast, M. Sanghadasa, and S. Priya, Sol. RRL **2**, 1800052 (2018).

[33] V. T. Tiong, N. D. Pham, T. Wang, T. Zhu, X. Zhao, Y. Zhang, Q. Shen, J. Bell, L. Hu, S. Dai, and H. Wang, Adv. Funct. Mater. **28**, 1705545 (2018).

[34] P. Chen, Y. Bai, S. Wang, M. Lyu, J.-H. Yun, and L. Wang, Adv. Funct. Mater. **28**, 1706923 (2018).

[35] J. Zhang, D. Bai, Z. Jin, H. Bian, K. Wang, J. Sun, Q. Wang, and S. F. Liu, Adv. Energy Mater. **8**, 1703246 (2018).

[36] L. Wan, X. Li, C. Song, Y. He, and W. Zhang, Sol. Energy Mater. Sol. Cells **191**, 437 (2019).

[37] W. Dai, S. Xu, J. Zhou, J. Hu, K. Huang, and M. Xu, Sol. Energy Mater. Sol. Cells **192**, 140 (2019).

[38] O. O. Johnson, P. E. Olutuase, and O. E. Oyewande, J. Phys.: Conf. Ser. **1299**, 012129 (2019).

[39] N. K. Noel, S. D. Stranks, A. Abate, C. Wehrenfennig, S. Guarnera, A.-A. Haghighirad, A. Sadhanala, G. E. Eperon, S. K. Pathak, M. B. Johnston, A. Petrozza, L. M. Herz, and H. J. Snaith, Energy Environ. Sci. **7**, 3061 (2014).

[40] S. Shao, J. Liu, G. Portale, H.-H. Fang, G. R. Blake, G. H. ten Brink, L. J. A. Koster, and M. A. Loi, Adv. Energy Mater. **8**, 1702019 (2018).

[41] M. Roknuzzaman, K. K. Ostrikov, K. Chandula Wasalathilake, C. Yan, H. Wang, and T. Tesfamichael, Org. Electron. **59**, 99 (2018).

[42] I. Kopacic, B. Friesenbichler, S. F. Hoefler, B. Kunert, H. Plank, T. Rath, and G. Trimmel, ACS Appl. Energy Mater. **1**, 343 (2018).

[43] H. Siddiqui, Mater. Lett. **249**, 99 (2019).

[44] M. Roknuzzaman, C. Zhang, K. K. Ostrikov, A. Du, H. Wang, L. Wang, and T. Tesfamichael, Sci. Rep. **9**, 718 (2019).

[45] F. Igbari, Z. K. Wang, and L. S. Liao, Adv. Energy Mater. **9**, 1803150 (2019).

[46] J. Zhou, X. Rong, M. S. Molokeev, X. Zhang, and Z. Xia, J. Mater. Chem. A **6**, 2346 (2018).

[47] Z. Deng, F. Wei, S. Sun, G. Kieslich, A. K. Cheetham, and P. D. Bristowe, J. Mater. Chem. A **4**, 12025 (2016).

[48] F. Wei, Z. Deng, S. Sun, F. Xie, G. Kieslich, D. M. Evans, M. A. Carpenter, P. D. Bristowe, and A. K. Cheetham, Mater. Horizons **3**, 328 (2016).

[49] S. Zhao, K. Yamamoto, S. Iikubo, S. Hayase, and T. Ma, J. Phys. Chem. Solids **117**, 117 (2018).

[50] G. Volonakis, A. A. Haghighirad, R. L. Milot, W. H. Sio, M. R. Filip, B. Wenger, M. B. Johnston, L. M. Herz, H. J. Snaith, and F. Giustino, J. Phys. Chem. Lett. **8**, 772 (2017).

[51] J. Zhou, Z. Xia, M. S. Molokeev, X. Zhang, D. Peng, and Q. Liu, J. Mater. Chem. A **5**, 15031 (2017).

[52] J. C. Dahl, W. T. Osowiecki, Y. Cai, J. K. Swabeck, Y. Bekenstein, M. Asta, E. M. Chan, and A. P. Alivisatos, Chem. Mater. **31**, 3134 (2019).

[53] K. N. N. Nandha and A. Nag, Chem. Commun. **54**, 5205 (2018).

[54] F. Liu, D. Marongiu, R. Pau, V. Sarritzu, Q. Wang, S. Lai, A. G. Lehmann, F. Quochi, M. Saba, A. Mura, G. Bongiovanni, A. Mattoni, C. Caddeo, A. Bosin, and A. Filippetti, EcoMat **2**, e12017 (2020).

[55] W. Meng, X. Wang, Z. Xiao, J. Wang, D. B. Mitzi, and Y. Yan, J. Phys. Chem. Lett. **8**, 2999 (2017).

[56] N. Chen, T. Cai, W. Li, K. Hills-Kimball, H. Yang, M. Que, Y. Nagaoka, Z. Liu, D. Yang, A. Dong, C.-Y. Xu, R. Zia, and O. Chen, ACS Appl. Mater. Interfaces **11**, 16855 (2019).

[57] A. H. Slavney, L. Leppert, D. Bartesaghi, A. Gold-Parker, M. F. Toney, T. J. Savenije, J. B. Neaton, and H. I. Karunadasa, J. Am. Chem. Soc. **139**, 5015 (2017).

[58] F. Locardi, M. Cirignano, D. Baranov, Z. Dang, M. Prato, F. Drago, M. Ferretti, V. Pinchetti, M. Fanciulli, S. Brovelli,

L. De Trizio, and L. Manna, J. Am. Chem. Soc. **140**, 12989 (2018).

[59] J. Luo, X. Wang, S. Li, J. Liu, Y. Guo, G. Niu, L. Yao, Y. Fu, L. Gao, Q. Dong, C. Zhao, M. Leng, F. Ma, W. Liang, L. Wang, S. Jin, J. Han, L. Zhang, J. Etheridge, J. Wang, Y. Yan, E. H. Sargent, and J. Tang, Nature (London) **563**, 541 (2018).

[60] Y. Liu, Y. Jing, J. Zhao, Q. Liu, and Z. Xia, Chem. Mater. **31**, 3333 (2019).

[61] O. Kolebaje, O. Popoola, M. A. Khan, and O. Oyewande, Chaos, Solitons Fractals **139**, 109970 (2020).

[62] O. E. Oyewande, O. D. Olabiyi, and M. L. Akinyemi, J. Phys.: Conf. Ser. **1299**, 012115 (2019).

[63] E. Yewande, M. Neal, and R. Low, Mol. Phys. **107**, 281 (2009).

[64] A. Akinpelu, O. E. Oyewande, Adaeze, A. T. Emuobor, C. Olawole, I. Ogunrionola, and O. O. Paul, J. Phys.: Conf. Ser. **1299**, 012022 (2019).

[65] O. E. Oyewande, I. B. Babalola, and M. Usikalu, J. Phys.: Conf. Ser. **1299**, 012120 (2019).

[66] M. Kibbou, Y. Benhouria, M. Boujnah, I. Essaoudi, A. Ainane, and R. Ahuja, J. Magn. Magn. Mater. **495**, 165833 (2020).

[67] E. O. Yewande, R. Kree, and A. K. Hartmann, Phys. Rev. B **73**, 115434 (2006).

[68] J. D. Femi-Oyetoro and O. E. Oyewande, J. Nano- Electron. Phys. **7**, 01002 (2015).

[69] O. E. Oyewande and A. Akinpelu, Nucl. Instrum. Methods Phys. Res., Sect. B **434**, 102 (2018).

[70] O. E. Oyewande and A. Akinpelu, IOP Conf. Ser. Earth Environ. Sci. **173**, 012045 (2018).

[71] O. E. Oyewande, Commun. Theor. Phys. **58**, 165 (2012).

[72] E. O. Yewande, R. Kree, and A. K. Hartmann, Phys. Rev. B **75**, 155325 (2007).

[73] O. El Rhazouani and A. Benyoussef, J. Magn. Magn. Mater. **446**, 166 (2018).

[74] E. O. Yewande, A. K. Hartmann, and R. Kree, Phys. Rev. B **71**, 195405 (2005).

[75] T. Atsue, I. B. Ogunniranye, and O. E. Oyewande, Electron. Struct. **2**, 045002 (2020).

[76] Y. Jiao, S. Zhang, Z. Yang, and G. Lu, Comput. Theor. Chem. **1148**, 55 (2019).

[77] S. Yamanaka, K. Kurosaki, A. Charoenphakdee, H. Mastumoto, and H. Muta, MRS Proc. **1044**, 1044U08-02 (2007).

[78] V. Kumar, K. Kumar, H. Jeon, T. Kang, D. Lee, and S. Kumar, J. Phys. Chem. Solids **124**, 1 (2019).

[79] N. J. Ramer and A. M. Rappe, Phys. Rev. B **62**, R743 (2000).

[80] N. Ramer and A. Rappe, J. Phys. Chem. Solids **61**, 315 (2000).

[81] C.-J. Yu and H. Emmerich, J. Phys.: Condens. Matter **19**, 306203 (2007).

[82] P. Giannozzi *et al.*, J. Phys.: Condens. Matter **21**, 395502 (2009).

[83] P. Giannozzi *et al.*, J. Phys.: Condens. Matter **29**, 465901 (2017).

[84] J. P. Perdew, K. Burke, and M. Ernzerhof, Phys. Rev. Lett. **77**, 3865 (1996).

[85] J. P. Perdew, M. Ernzerhof, and K. Burke, J. Chem. Phys. **105**, 9982 (1996).

[86] D. R. Hamann, Phys. Rev. B **88**, 085117 (2013).

[87] H. J. Monkhorst and J. D. Pack, Phys. Rev. B **13**, 5188 (1976).

[88] T. H. Fischer and J. Almlöf, J. Phys. Chem. **96**, 9768 (1992).

[89] I. Timrov, N. Vast, R. Gebauer, and S. Baroni, Phys. Rev. B **88**, 064301 (2013).

[90] I. Timrov, N. Vast, R. Gebauer, and S. Baroni, Comput. Phys. Commun. **196**, 460 (2015).

[91] S. Sharma, J. K. Dewhurst, and C. Ambrosch-Draxl, Phys. Rev. B **67**, 165332 (2003).

[92] R. D. Shannon, Acta Crystallogr., Sect. A **32**, 751 (1976).

[93] E. Meyer, D. Mutukwa, N. Zingwe, and R. Taziwa, Metals (Basel, Switz.). **8**, 667 (2018).

[94] C.-j. Yu, J. Phys. Energy **1**, 022001 (2019).

[95] C. J. Bartel, C. Sutton, B. R. Goldsmith, R. Ouyang, C. B. Musgrave, L. M. Ghiringhelli, and M. Scheffler, Sci. Adv. **5**, eaav0693 (2019).

[96] Z. Xiao, K.-Z. Du, W. Meng, D. B. Mitzi, and Y. Yan, Angew. Chem. **129**, 12275 (2017).

[97] K. Momma and F. Izumi, J. Appl. Crystallogr. **44**, 1272 (2011).

[98] F. Birch, Phys. Rev. **71**, 809 (1947).

[99] D. Han, T. Zhang, M. Huang, D. Sun, M.-H. Du, and S. Chen, APL Mater. **6**, 084902 (2018).

[100] H. Q. Pham, R. J. Holmes, E. S. Aydil, and L. Gagliardi, Nanoscale **11**, 11173 (2019).

[101] L. Leppert, T. Rangel, and J. B. Neaton, Phys. Rev. Mater. **3**, 103803 (2019).

[102] Z.-h. Yang and C. A. Ullrich, Phys. Rev. B **87**, 195204 (2013).

[103] A. Marini, C. Hogan, M. Grüning, and D. Varsano, Comput. Phys. Commun. **180**, 1392 (2009).